Supporting Information for

Guided phase transition for mitigating voltage hysteresis of iron fluoride cathode materials in lithium-ion batteries

Hyoi Jo,[‡a] Minjeong Gong[‡ b], Se Young Kim[c], Dong-Hwa Seo[*b] and Sung-Kyun Jung[*a]

Affiliation

a. Department of Energy Engineering, School of Energy and Chemical Engineering, Ulsan National Institute of Science and Technology (UNIST), Ulsan 44919, Republic of Korea

b. Department of Materials Science and Engineering, Korea Advanced Institute of Science and Technology (KAIST); 291 Daehak-ro, Yuseong-gu, Daejeon 34141, Republic of Korea

c. Energy Storage Research Center, Korea Institute of Science and Technology (KIST), 14 Gil 5 Hwarang-ro, Seongbuk-gu, Seoul, 02792 Republic of Korea

* Corresponding to: dseo@kaist.ac.kr and skjung@unist.ac.kr

‡ These authors contributed equally to this work.

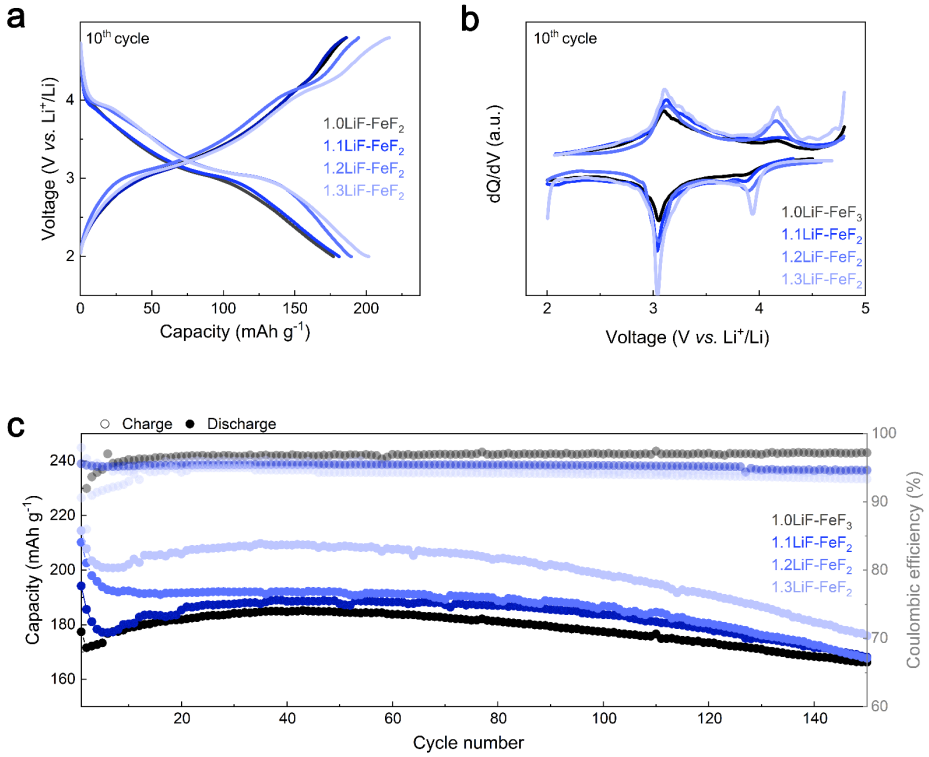

Supplementary Fig. S1. (a-c) Comparison of 10th charge/discharge profiles, differential analysis of voltage profiles, and cycle performance for various amounts of LiF at 25 °C and 20 mA g^{-1} current density.

Supplementary Note 1. Comparison of Electrochemical Profiles Based on LiF Content in LiF-FeF_2 Nanocomposites

The electrochemical performance of LiF-FeF_2 nanocomposites with varying molar ratios of LiF was systematically evaluated (Supplementary Fig. S1). An increase in the LiF content corresponded with a notable enhancement in capacity, as well as a more pronounced plateau at 4V. This phenomenon is likely due to the augmented formation of new polymorphs resulting from the increased interaction between LiF and FeF_2. Nevertheless, when the concentration of LiF, which is inherently an insulating material, surpasses a critical threshold, a significant decline in capacity is observed.

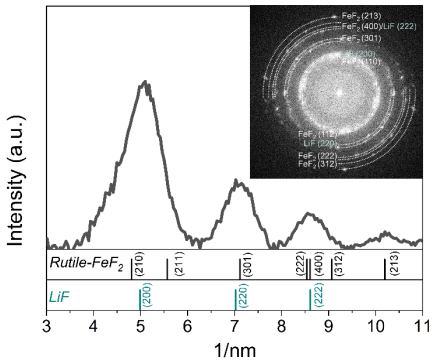

Supplementary Fig. S2. Azimuthal integration of FFT pattern (Fig. 1b) for LiF-FeF_2 nanocomposite.

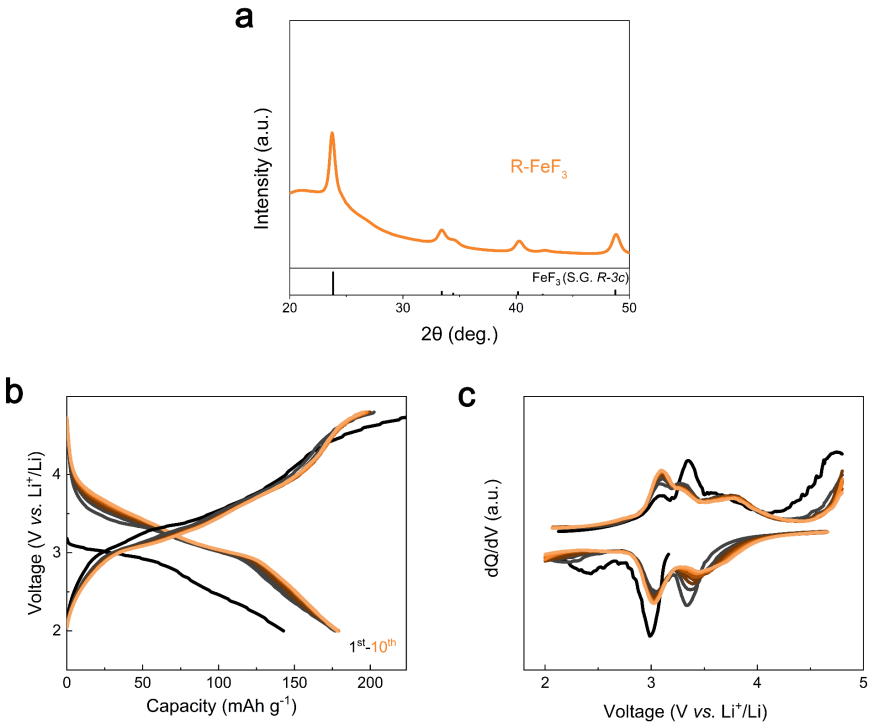

Supplementary Fig. S3. (a) Powder X-ray diffraction patterns of the rhombohedral FeF_3 (R-FeF_3). **(b)** Electrochemical profile of R-FeF_3 at 25 °C and current density of 20 mA g^{-1}. **(c)** Differential analysis of the voltage profile.

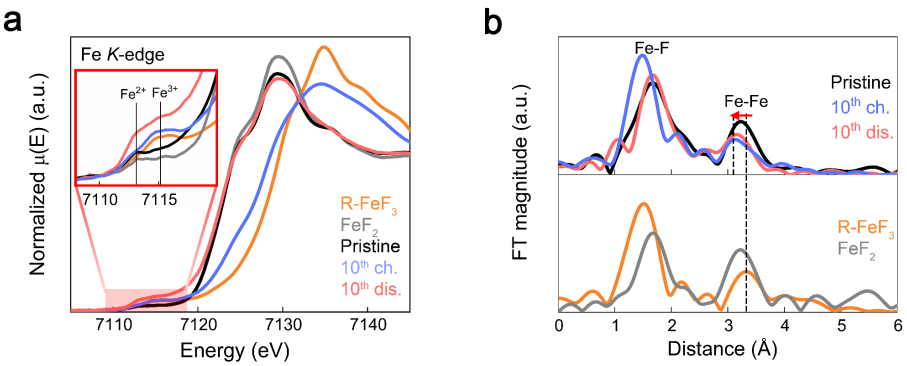

Supplementary Fig. S4. (a, b) *Ex-situ* XANES and EXAFS spectra of the Fe *K*-edge for pristine and 10th charged/discharged state. The inset shows an expanded view of the pre-edge region.

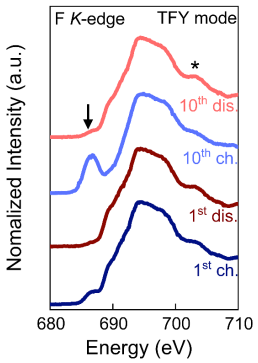

Supplementary Fig. S5. F *K*-edge XAS spectra of the LiF-FeF_2 in total fluorescence yield (TFY) at 1st and 10th cycles. The asterisk is the peak corresponding to LiF.

Supplementary Note 2. Origin of Fluoride Ions in the Formation of T-FeF_3

To investigate the origin of fluoride ions (F^-) in the formation of tetragonal FeF_3 (T-FeF_3), F K-edge spectra analysis was conducted (Supplementary Fig. S5). The F *K*-edge spectra in total fluorescence yield (TFY) mode for the 1st and 10th cycles show a distinct pre-edge peak around 684.0 eV that becomes more prominent upon cycling. This peak, commonly observed in highly oxidized iron fluorides and oxyfluorides, relates to the transition of F 1s to 2p orbitals hybridized with Fe 3d orbitals[1–5], suggesting the formation of $Fe^{3+}F_3$. For $Fe^{3+}F_3$ to form electrochemically, F ions from LiF must act as charge neutralizers during charging process. Since the electrochemical measurements were conducted in the presence of F ion-containing binders and electrolytes (Fig. 1c), we confirmed the electrochemical profile in the absence environment of other F ion sources except LiF (Supplementary Fig. S6). The evolution of the 4 V plateau was observed without significant changes in the electrochemical profile. This suggests that the reaction between LiF and FeF_2 forms an electrochemically active FeF_3 with a tetragonal-like polymorph.

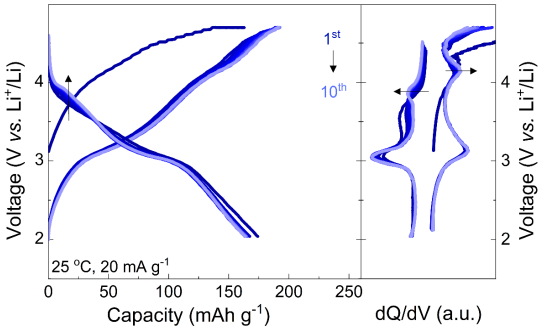

Supplementary Fig. S6. Electrochemical profile of LiF-FeF_2 nanocomposite without additional fluorine sources other than LiF.

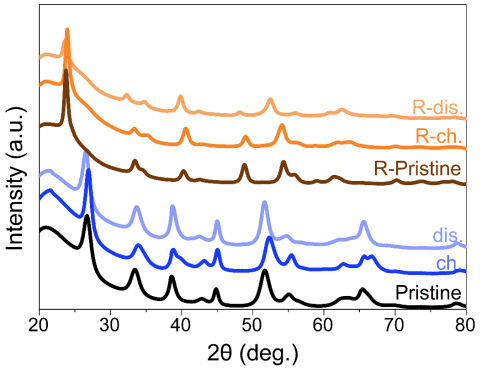

Supplementary Fig. S7. *Ex-situ* XRD patterns of LiF-FeF_2 and R-FeF_3 electrodes at pristine and 10^{th} charged/discharged states.

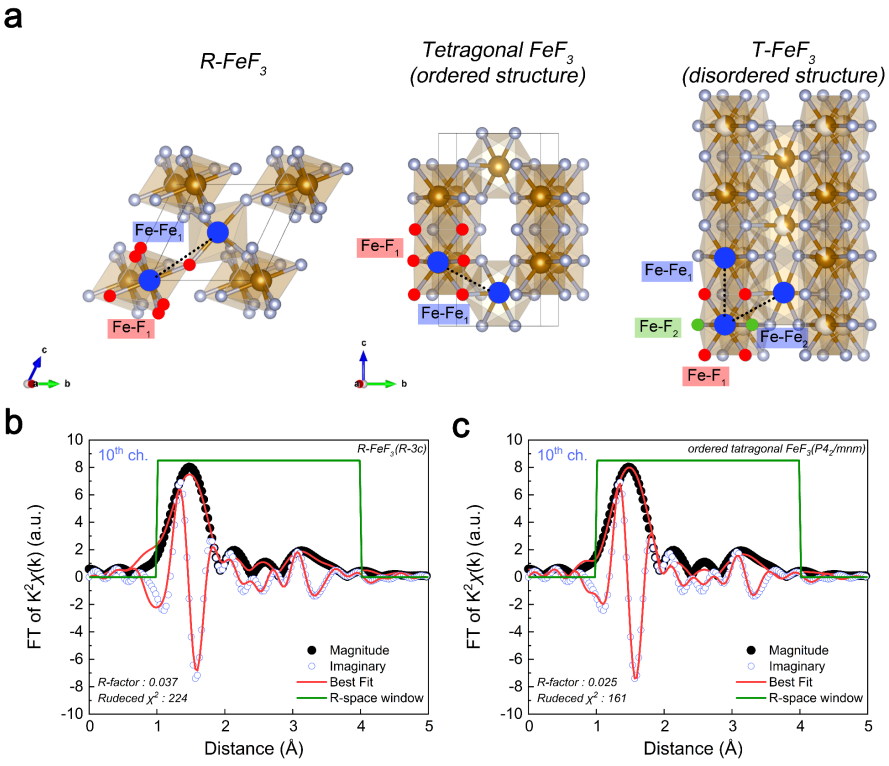

Supplementary Fig. S8. (a) Crystal structures of ordered tetragonal FeF_3, T-FeF_3 (disordered structure), and R-FeF_3. Brown and silver balls indicate Fe and F ions, respectively. Fourier transformed magnitude (black), imaginary part (blue), and best fit (red) using **(b)** the R-FeF_3 model and **(c)** the ordered tetragonal FeF_3 model for the 10th charged state electrode**.** (See Supplementary Table S2.)

Supplementary Note 3. Identification of Electrochemically Induced Polymorphs in the Local Environment

The tetragonal structure of FeF_3 derived from $Li_{0.5}FeF_3$ has been reported in two forms based on the ordering of Fe: the ordered tetragonal FeF_3, where Fe is occupied at the 4e site, and the disordered tetragonal FeF_3, where Fe is randomly distributed at the 2a and 4e sites[6]. The arrangement of Fe affects the local environment of Fe and, consequently, the EXAFS spectrum[7]. In the EXAFS spectrum of the 10th charged state of LiF-FeF_2 shown in Supplementary Fig. S4b, a shorter Fe-Fe distance is observed compared to R-FeF_3. Both ordered tetragonal FeF_3 and R-FeF_3 exhibit a Fe-Fe distance of ~3.7 Å, while disordered tetragonal FeF_3 shows Fe-Fe distances of 3.16 Å and 3.69 Å. These differences can be attributed to structural variations among ordered tetragonal FeF_3, disordered tetragonal FeF_3, and R-FeF_3. To elucidate the structure induced from LiF-FeF_2, we performed EXAFS fitting for each structure (Supplementary Fig. S8a). The disordered tetragonal FeF_3 (Fig. 1f) exhibited significantly lower reduced χ^2 and R-factor values compared to R-FeF_3 and ordered tetragonal FeF_3

(Supplementary Figs. S8b and S8c), indicating that the local environment is more consistent with the disordered tetragonal structure.

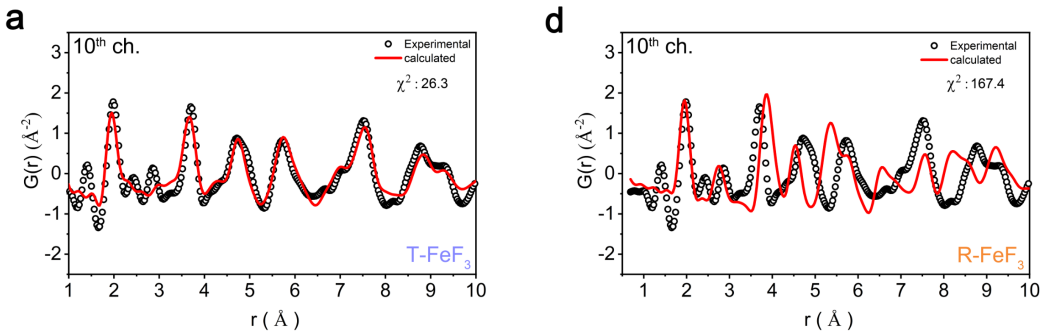

Supplementary Fig. S9. **(a,b)** Comparison between the T-FeF_3 and R-FeF_3 structures for the PDF of the 10th charge state of LiF-FeF_2.

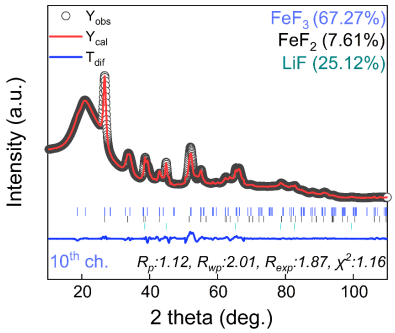

Supplementary Fig. S10. Rietveld refinement of the XRD data (λ = 1.5406 Å) of the 10th charged state. (See Supplementary Table S3.)

Supplementary Note 4. Identification of a Tetragonal Polymorph Electrochemically Derived from LiF-FeF_2

Previous studies have reported the electrochemical induction of a tetragonal FeF_3 structure from $Li_{0.5}FeF_3$[6]. The reported tetragonal FeF_3 shares the same anion framework as FeF_2 (*P4$_2$/mnm*) but differs in the occupancy of Fe sites. Based on the similarity between the XRD pattern of the 10th charged state (Supplementary Fig. S7) and that of FeF_2, along with the characteristic 4 V plateau observed in the charge/discharge profile (Fig. 1c), we identified tetragonal FeF_3 as a potential polymorph electrochemically induced from LiF-FeF_2. Rietveld refinement of the XRD pattern at the 10th charged state, where the 4 V plateau is prominently formed, confirmed a good fit with the tetragonal FeF_3 structure (Supplementary Fig. S10).

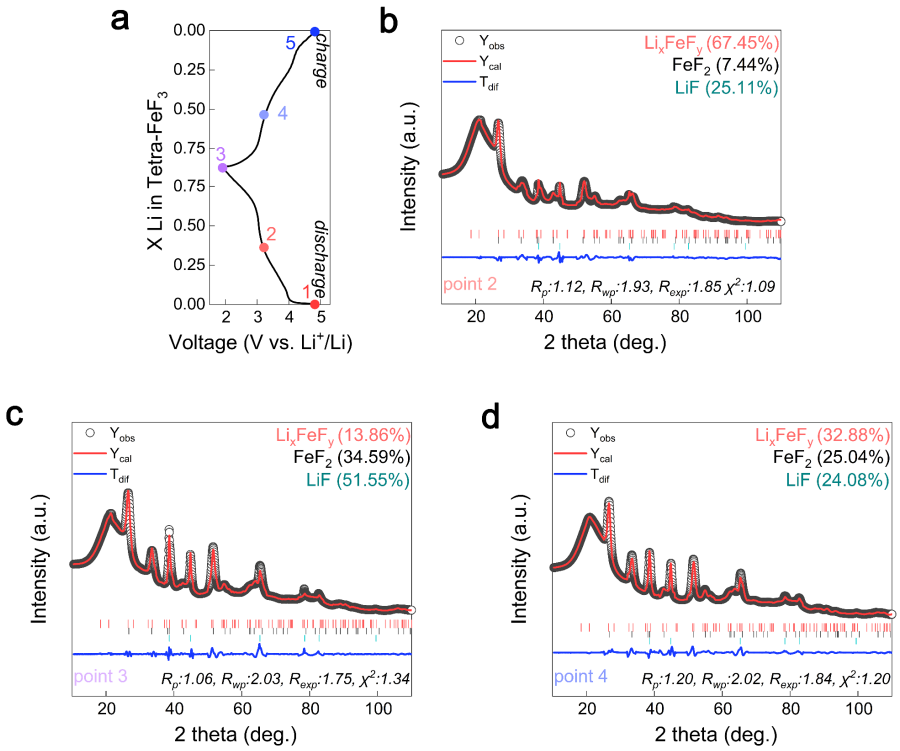

Supplementary Fig. S11. (a) Voltage-time profile of T-FeF_3. Rietveld refinement of the XRD data (λ = 1.5406 Å) of **(b)** half-discharged state (point 2), **(c)** discharged state (point 3), and **(d)** half-charged state (point 4). (See Supplementary Table S4.)

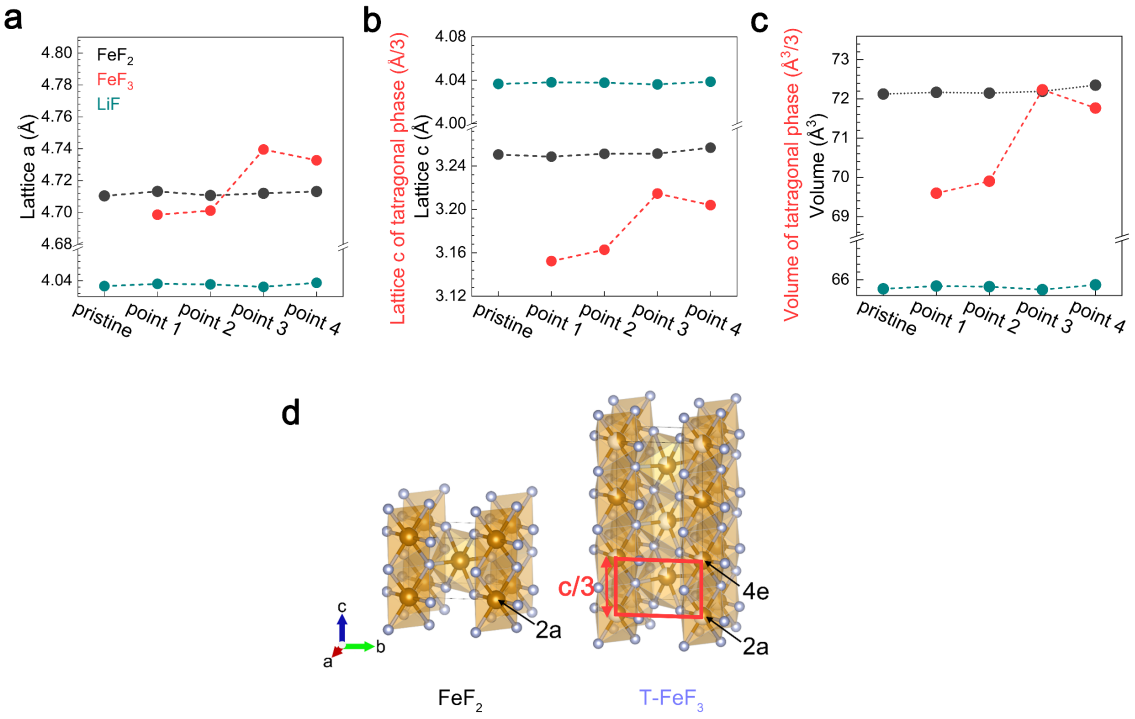

Supplementary Fig. S12. Comparison of refined crystallographic parameters at each voltage. **(a)** Lattice a parameter, **(b)** lattice c parameter, and **(c)** volume. **(b)** Crystal structure of T-FeF_3 and FeF_2. Since T-FeF_3 is similar to a three-fold stacking of the FeF_2 anion framework, the c lattice parameter and volume were expressed as Å/3 and $Å^3/3$ to compare with FeF_2. (See Supplementary Table S3 and S4.)

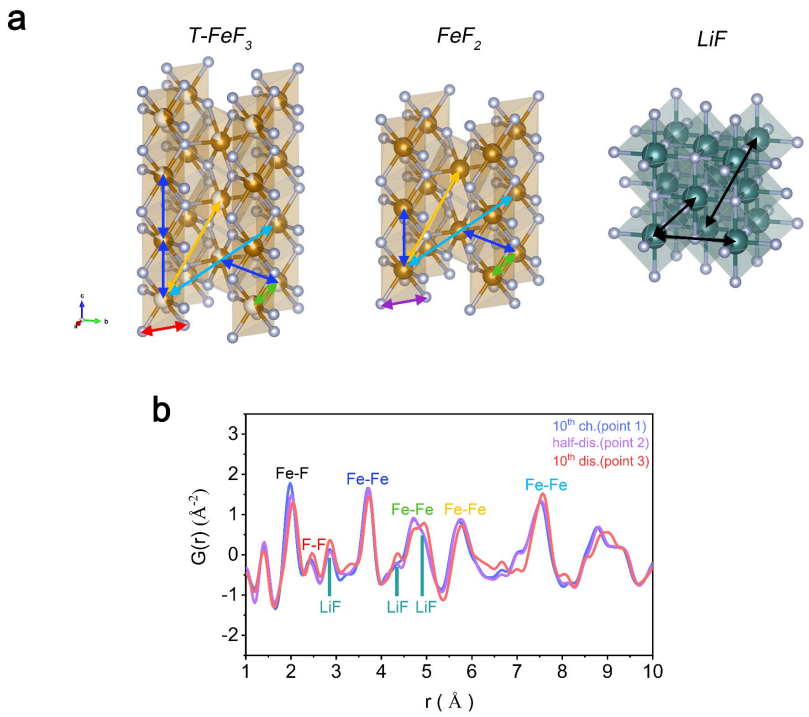

Supplementary Fig. S13. (a) Crystal structures of T-FeF_3, FeF_2, and LiF. Each arrow corresponds to each peak in the PDF. **(b)** PDF comparison for 10th charge (point 1), half-discharge (point 2), and 10th discharge (point 3).

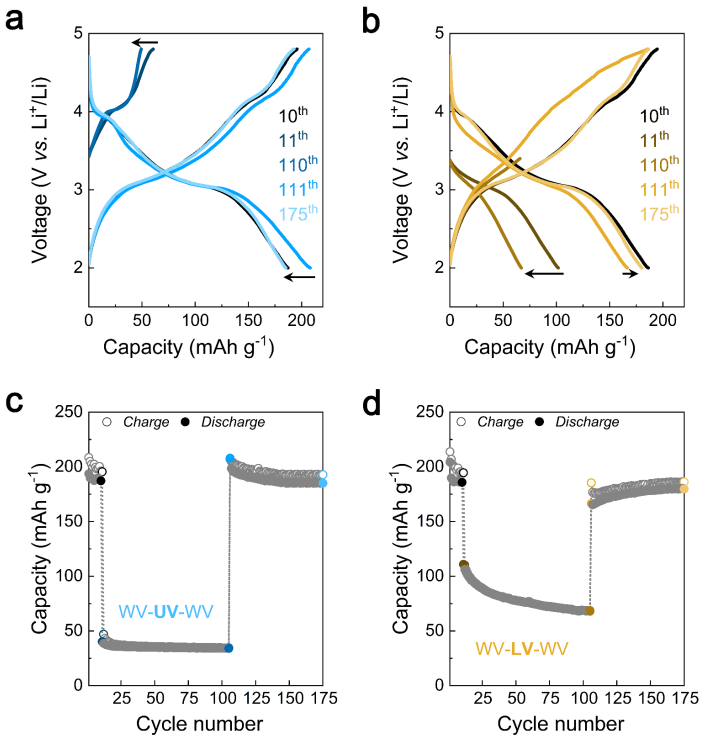

Supplementary Fig. S14. Voltage profile and cycle performance of T-FeF_3 in the order of **(a, c)** WV-UV-WV range and **(b, d)** WV-LV-WV range.

Supplementary Note 5. Evaluation of the Reversibility of T-FeF_3

Supplementary Fig. S14 demonstrates the reversibility across different voltage ranges after the initial 10 cycles required to form T-FeF_3. At the 100th cycle, the wide voltage (WV, Supplementary Fig. S1c) and upper voltage ranges (UV) show excellent capacity retention of 99 % and 93 %, respectively, while the lower voltage range (LV) exhibits relatively poor capacity retention of 69 %. The excellent reversibility in the UV and the rapid capacity decay in the LV suggest that the reaction mechanism of T-FeF_3 proceeds through Li^+ insertion and conversion reaction.

During the charging process, the phase fraction changes gradually through points 4 and 5, unlike the stepwise changes observed during discharge (Fig. 2c). The formation of T-FeF_3 from LiF and FeF_2 requires the splitting of LiF:

$$LiF + FeF_2 \rightarrow FeF_3 + Li^+$$

LiF splitting requires a high-voltage environment[8–12]. Insufficient LiF splitting in the LV may lead to incomplete formation of T-FeF_3 and accumulation of inactive LiF, resulting in capacity decay. To verify insufficient LiF splitting in the LV, reversibility was checked in the UV and LV, followed by a cycle in the WV (Supplementary Fig. S14). The electrochemical profile and capacity in UV remained almost identical to the 10th cycle when re-measured in the WV. In

contrast, the LV showed the absence of the 4 V plateau and lower capacity compared to the 10^{th} cycle. However, with continued cycling in the WV range, the evolution of the 4 V plateau and an increase in capacity were observed. The absence of the 4 V plateau and lower capacity in the LV suggest failure to form T-FeF_3 due to insufficient LiF splitting, and the evolution of the 4 V plateau and capacity increase in the WV with additional cycling indicate the successful formation of T-FeF_3 under high-voltage operation. These characteristics of electrochemical behavior across various voltage ranges provide further evidence that T-FeF_3 undergoes both insertion and conversion reaction mechanisms.

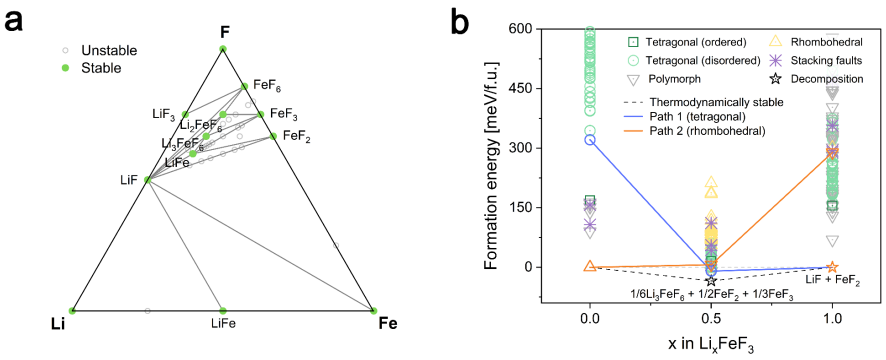

Supplementary Fig. S15. (a) Phase diagram of Li-Fe-F system. **(b)** The formation energies as a function of Li contents with all considered structures (ordered and disordered tetragonal, rhombohedral, stacking faulted[13], various polymorphs of each composition from materials project[14]. The dashed line is the convex hull of the formation energies, and the red and navy solid lines are the suggested reaction path according to the host structure (tetragonal and rhombohedral structure).

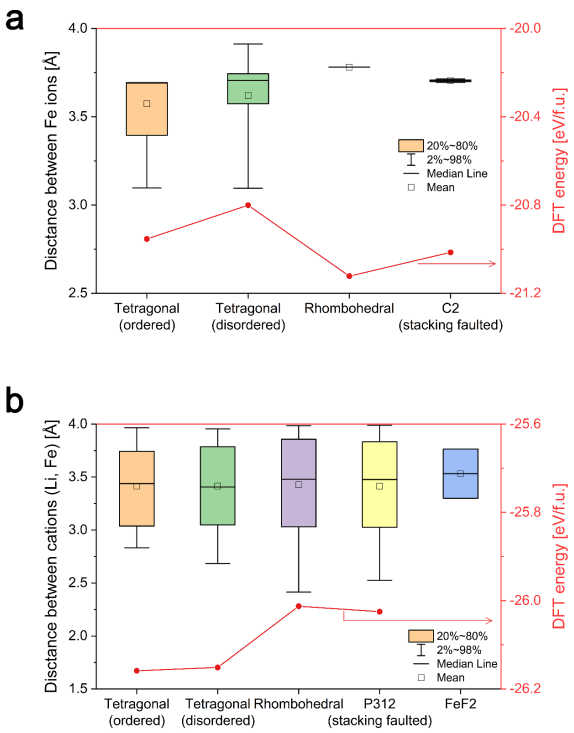

Supplementary Fig. S16. The distance between cations (Li and Fe) and calculated energy of each structure **(a)** the fully delithiated state (x=0), **(b)** the fully lithiated state (x=1).

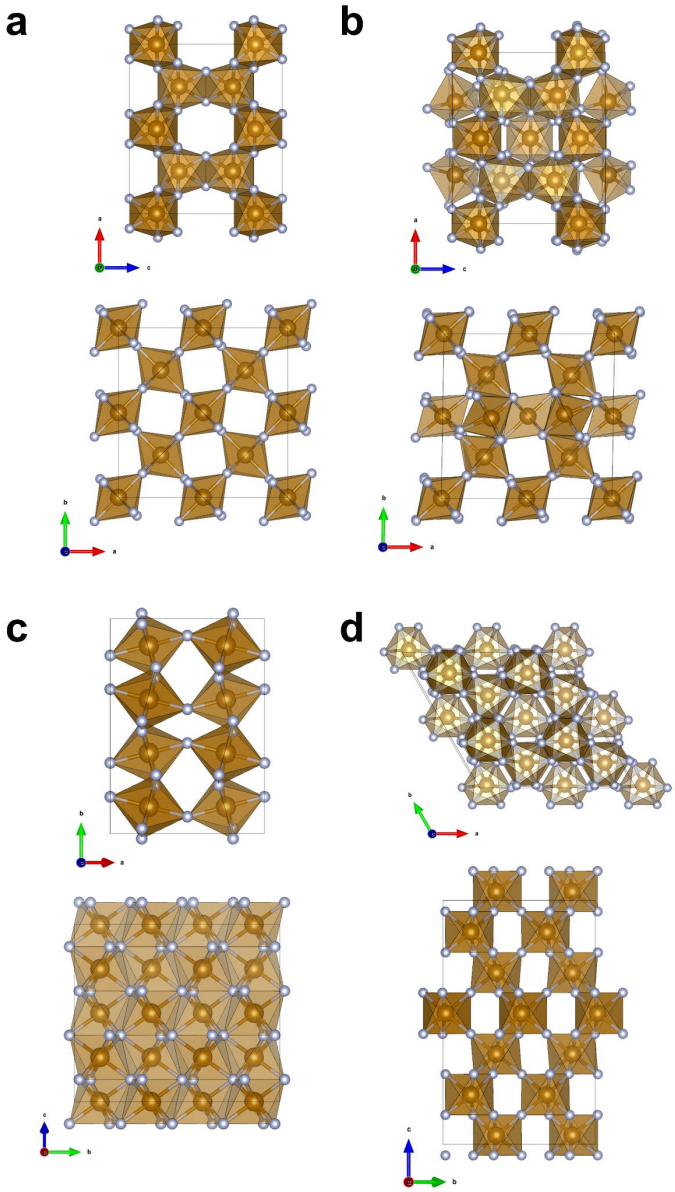

Supplementary Fig. S17. The structures of FeF_3 polymorphs **(a)** ordered tetragonal, **(b)** disordered tetragonal, **(c)** rhombohedral, and **(d)** stacking faulted (P312) structure. Fe, F are in gold, and silver balls, respectively.

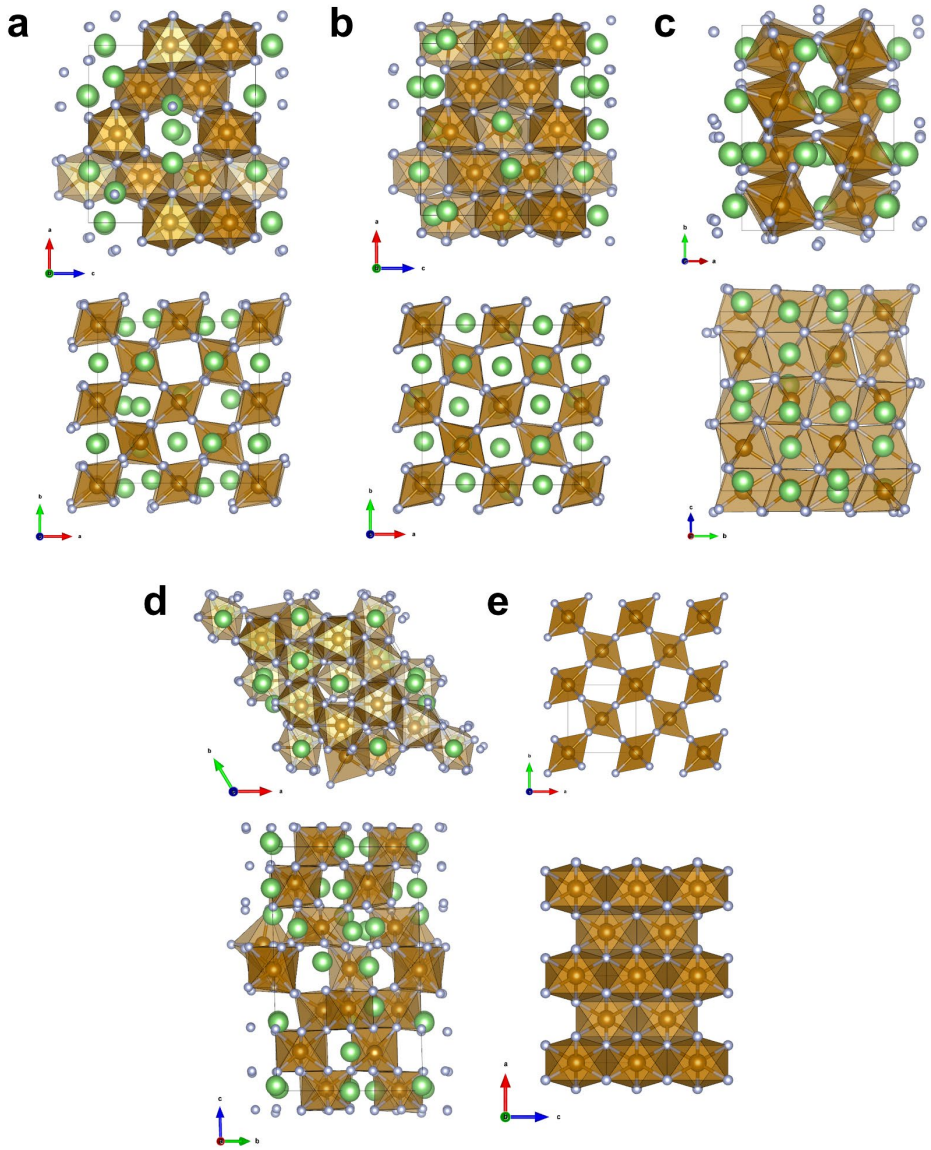

Supplementary Fig. S18. The structures of $LiFeF_3$ polymorphs **(a)** ordered tetragonal, **(b)** disordered tetragonal, **(c)** rhombohedral, **(d)** stacking faulted (P312) structures. **(e)** FeF_2 is one of decomposition products of $LiFeF_3$. Li, Fe, F are in green, gold, and silver balls, respectively.

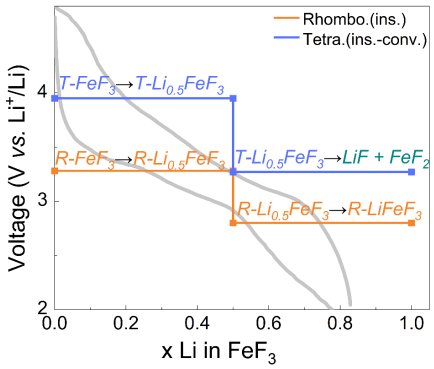

Supplementary Fig. S19. Experimentally measured voltage profile and DFT calculated reaction voltage for R-FeF_3 at different states of lithiation.

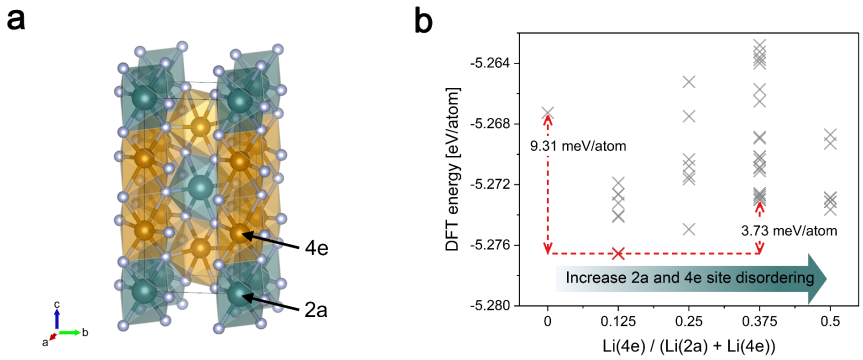

Supplementary Fig. S20. The Li and Fe site preference between 2a and 4e sites in tetragonal $Li_{0.5}FeF_3$ structure. **(a)** The crystal structure of ordered tetragonal $Li_{0.5}FeF_3$ ($P4_2/mnm$). Green, brown, and silver balls indicate Li, Fe, and F ions. **(b)** The DFT energy of tetragonal $Li_{0.5}FeF_3$ as a function of the fraction of Li occupancy in the 4e site. The red mark indicates the lowest energy among Li and Fe site-disordered structures**.**

Supplementary Note 6. Li and Fe Site Disordering in Tetragonal $Li_{0.5}FeF_3$

In the ordered tetragonal $Li_{0.5}FeF_3$ structure ($P4_2/mnm$), Li and Fe atoms are located at 2a and 4e sites, respectively. Our experimental results, along with previous reports[6], indicate that site disordering between Li and Fe atoms occurs during cycling (Supplementary Note 3 and Fig. S10). To investigate the stability of cation disordering, we generated Li and Fe site-disordered structures using enumeration techniques and obtained their energies through DFT calculations (Supplementary Fig. S20). The most stable configuration is a slightly disordered structure where 0.125 Li atoms occupy the 4e site and the rest occupy the 2a site. The energy difference between this most stable and ordered configurations is 9.31 meV/atom. Note that the Li and Fe site-disordered structure based on the previous report[6] is 3.73 meV/atom higher than our most stable configuration. Although this configuration is less stable than the most stable structure, their energy difference is quite small, thus, they can coexist due to entropy at room temperature.

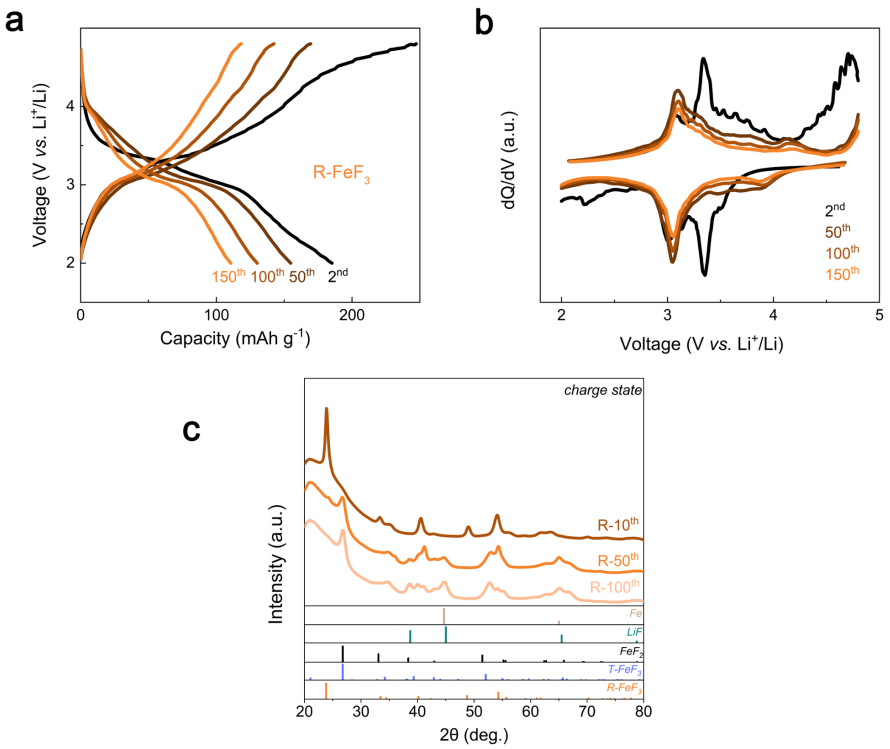

Supplementary Fig. S21. (a,b) Electrochemical profile and differential analysis of voltage profile according to long-term cycling of R-FeF_3 at 25 °C and 20 mA g^{-1} current density. (c) *ex-situ* XRD patterns for the 10th, 50th, and 100th charge states.

Supplementary Note 7. Irreversible Phase Transition of R-FeF_3 During Long-Term Cycling

Recent studies on the reaction mechanism of R-FeF_3 have reported that Li insertion into R-FeF_3 forms $Li_xFe_yF_3$, a structure deficient in Fe, leading to the irreversible phase displacement of FeF_2 into a tetragonal structure from the first discharge cycle[13]. Initially, the crystallinity of the displaced FeF_2 is low and is only detectable through PDF analysis. However, with repeated charge/discharge cycles, the accumulation of irreversible FeF_2 may become observed in XRD patterns. Long-term cycling experiments were performed to investigate the irreversible formation of FeF_2 (rcp-tcp transition) in the reaction mechanism of R-FeF_3.

As shown in Supplementary Fig. S21a, a gradual decrease in capacity is observed as cycling progresses. Interestingly, a slight 4 V plateau characteristic of T-FeF_3 emerges with continued cycling. If this electrochemical feature is due to the irreversible rcp-tcp transition, FeF_2 should be observable in the charged state. To confirm this, we examined *ex-situ* XRD patterns of the 50th and 100th charge states, where the 4 V redox peak starts to appear in dQ/dV and becomes more pronounced, respectively (Supplementary Fig. S21c and S21b). Up to the 10th cycle, the XRD pattern primarily exhibits rhombohedral structure peaks. However, as cycling progresses,

the main peak of the rhombohedral structure at 23.9° gradually diminishes. Conversely, the peak at 26.8° corresponding to the tetragonal structure (indicated by black arrows) becomes more prominent. Additionally, peaks corresponding to LiF and Fe metal (at 44.7°, indicated by green arrows) also emerge with continued cycling. These observations strongly support the inclusion of an irreversible rcp-tcp transition in the reaction pathway of R-FeF_3.

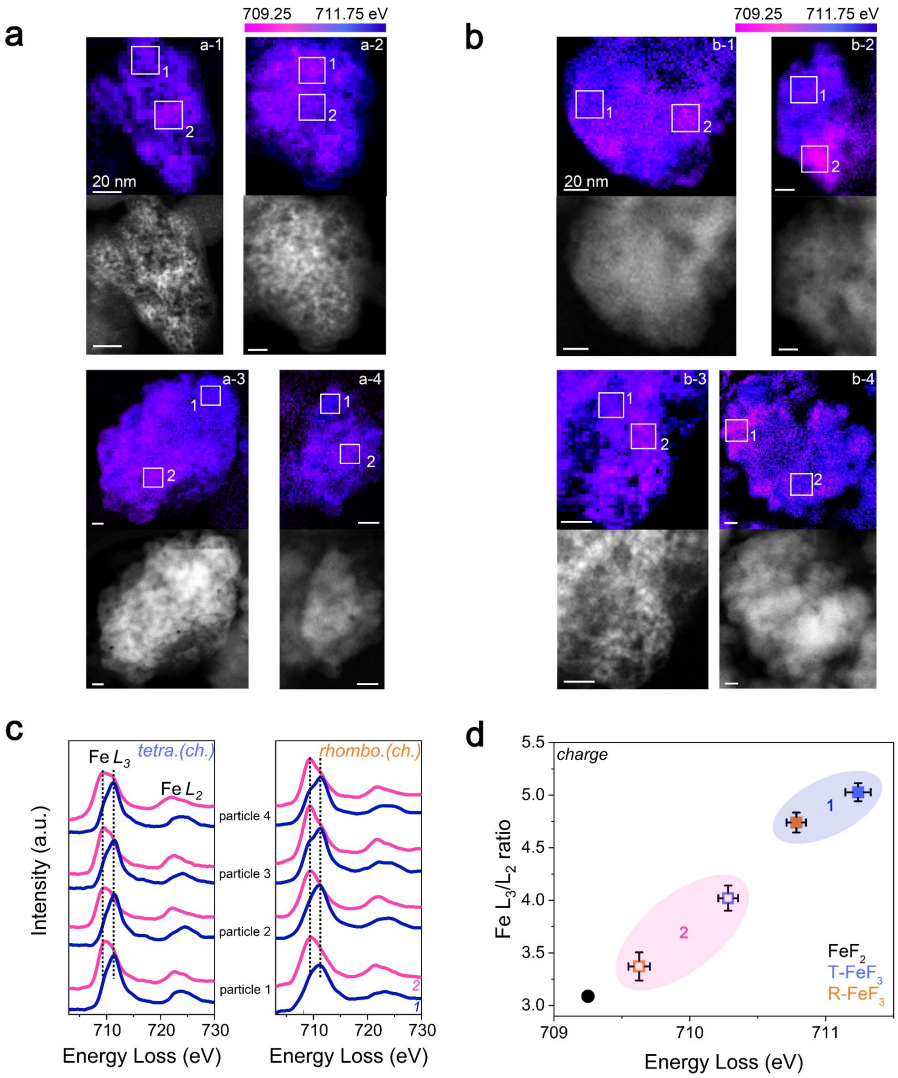

Supplementary Fig. S22. (a,b) STEM-EELS images of T-FeF_3 and R-FeF_3 at 10th charged state for the energy distribution of the Fe L_3-edge peak. **(c,d)** Fe L_3-edge peak energy and the L_3/L_2 ratio of T-FeF_3 and R-FeF_3 at 10th charged state.

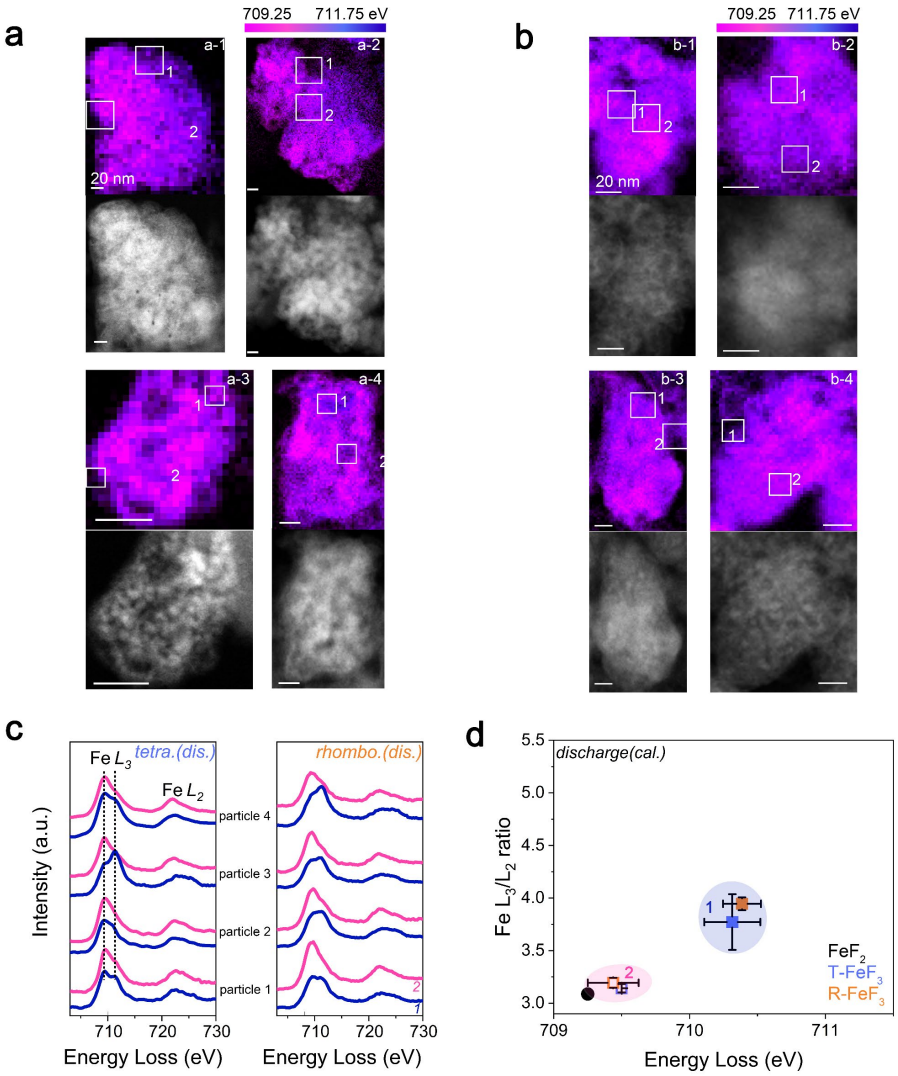

Supplementary Fig. S23. (a,b) STEM-EELS images of T-FeF_3 and R-FeF_3 at 10th discharged state for the energy distribution of the Fe L_3-edge peak. **(c,d)** Fe L_3-edge peak energy and the L_3/L_2 ratio of T-FeF_3 and R-FeF_3 at 10th discharged state.

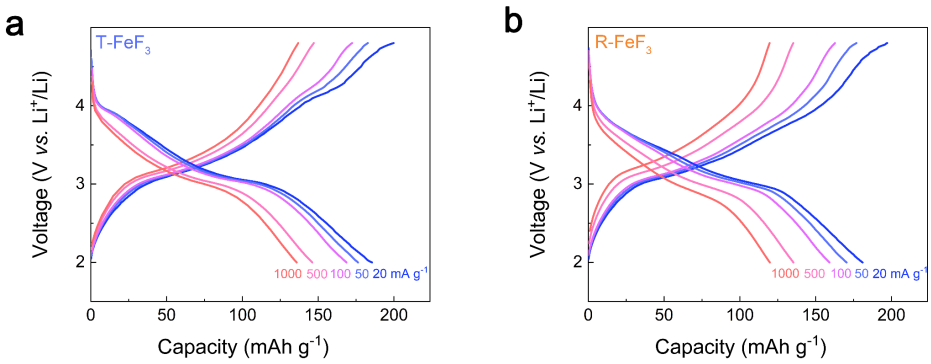

Supplementary Fig. S24. (a,b) Electrochemical profile of T-FeF_3 and R-FeF_3 corresponding charge/discharge profiles at various current densities.

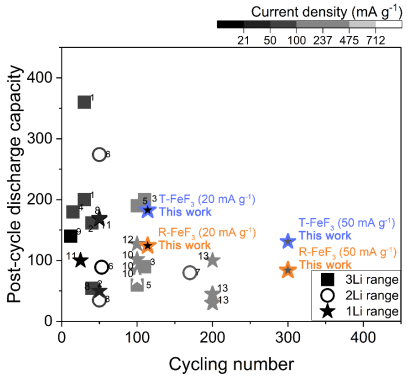

Supplementary Fig. S25. Comparison of post-cycle discharge capacity of iron fluoride materials composited with carbon and T-FeF_3. (See Supplementary Table S5.)

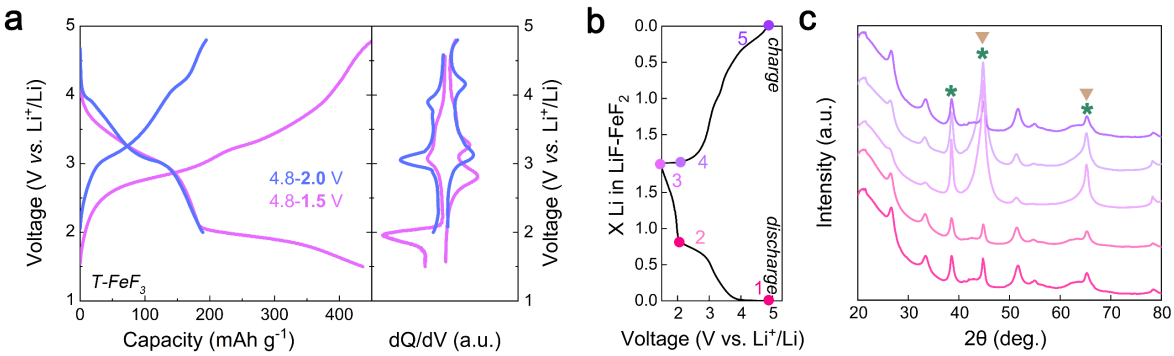

Supplementary Fig. S26. (a) The 10th charge/discharge profile and differential analysis of voltage profile for LiF-FeF_2 in various voltage ranges. Blue and pink are voltage profiles in the 4.8-2.0 V and 4.8-1.5 V voltage ranges, respectively. **(b)** Voltage profile depending on lithiation state in 4.8-1.5 V range. **(c)** XRD patterns of LiF-FeF_2 at different Li contents in 4.8-1.5 V range. Green stars and beige inverted triangles represent LiF and Fe metal, respectively.

Supplementary Note 8. Reaction Pathway of T-FeF_3 Under Deep Discharge Conditions

The electrochemically induced T-FeF_3 from LiF-FeF_2 exhibits a characteristic 4 V plateau in the voltage range of 4.8-2.0 V. However, this electrochemical feature is not observed when evaluating LiF-FeF_2 in the deep discharge voltage range (4.8-1.5 V) (Supplementary Figure S26a). To investigate the structural changes of LiF-FeF_2 during deep discharge, *ex-situ* XRD was measured at various voltages. As shown in Supplementary Fig. S26c, the diffraction pattern of the tetragonal phase is observed up to point 2. However, upon discharge to 1.5 V (point 3), distinct peaks corresponding to LiF (green asterisks) and Fe metal (beige inverted triangles) are clearly observed. The conversion to Fe metal at 1.5 V discharge is further confirmed through XAS analysis. Supplementary Fig. S27 displays the XANES and EXAFS spectra for the charge/discharge cycles of LiF-FeF_2 in the 4.8-2.0V and 4.8-1.5V ranges. The high-intensity pre-edge peak of the Fe *K*-edge in the discharged state (D-1.5V) is characteristic of Fe metal. In the EXAFS spectrum, peaks at 2.3 and 4.38 Å, corresponding to Fe metal, are prominently observed at D-1.5V. These results confirm the conversion to Fe metal under deep discharge conditions, a reaction pathway consistent with R-FeF_3 (Supplementary Fig. S28)[13,15–17].

Interestingly, T-FeF_3 is not formed in the charged state of the deep discharge voltage range (C-1.5V) (Supplementary Fig. S28). The Fe *K*-edge spectrum at C-1.5V does not shift back to the energy level observed at C-2.0V, and the Fe-F distance influenced by the oxidation state of Fe is 0.1 Å longer at C-1.5V compared to C-2.0V (Supplementary Fig. S27). This suggests that Fe was not oxidized as much at C-1.5V as at C-2.0V. As demonstrated in Supplementary Note 5, the formation of T-FeF_3 requires sufficient LiF splitting. However, the Fe metal produced at D-1.5V is highly stable, necessitating a substantial overpotential for LiF and Fe

to react and form iron fluoride[18,19]. Therefore, the absence of distinct T-FeF_3 at C-1.5V indicates insufficient LiF splitting.

To verify this, we first performed a deep discharge and then evaluated LiF-FeF_2 in an environment with sufficient LiF splitting (4.8-2.0 V) (Supplementary Fig. S31). As shown in Supplementary Fig. S31d and S31e, a 4 V plateau, a characteristic feature of T-FeF_3, is observed in the 30th cycle. This shows that T-FeF_3 can form under sufficient conditions for LiF splitting, even when starting from a deep discharge. However, the electrochemical protocol that performs deep discharge first has a less pronounced 4V plateau compared to the protocol that forms T-FeF_3 first (point 3 in Fig. 5a). In addition, the discharge capacity is 172.5 mAh g^{-1} (Supplementary Fig. S32), which is 19.1 mAh g^{-1} less than at point 3 in Fig. 5. Nevertheless, the capacity retention is superior to that of R-FeF_3, highlighting the importance of the T-FeF_3 formation.

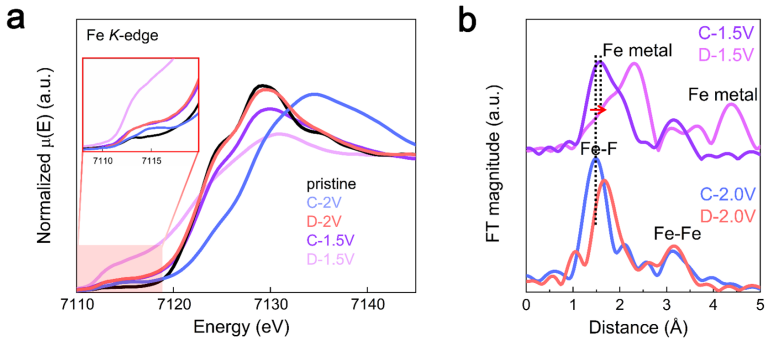

Supplementary Fig. S27. (a) XANES and **(b)** Fourier transform EXAFS spectra of the Fe *K*-edge for 10th charge/discharge states of LiF-FeF_2 in various voltage ranges. C and D represent charging and discharging states, and the right side represents the discharging cut-off voltage.

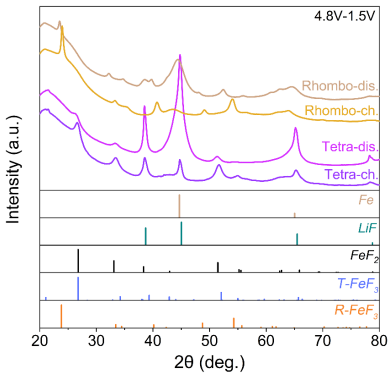

Supplementary Fig. S28. *Ex-situ* XRD patterns of LiF-FeF_2 and R-FeF_3 electrodes at charged/discharged states in the 4.8-1.5 V range.

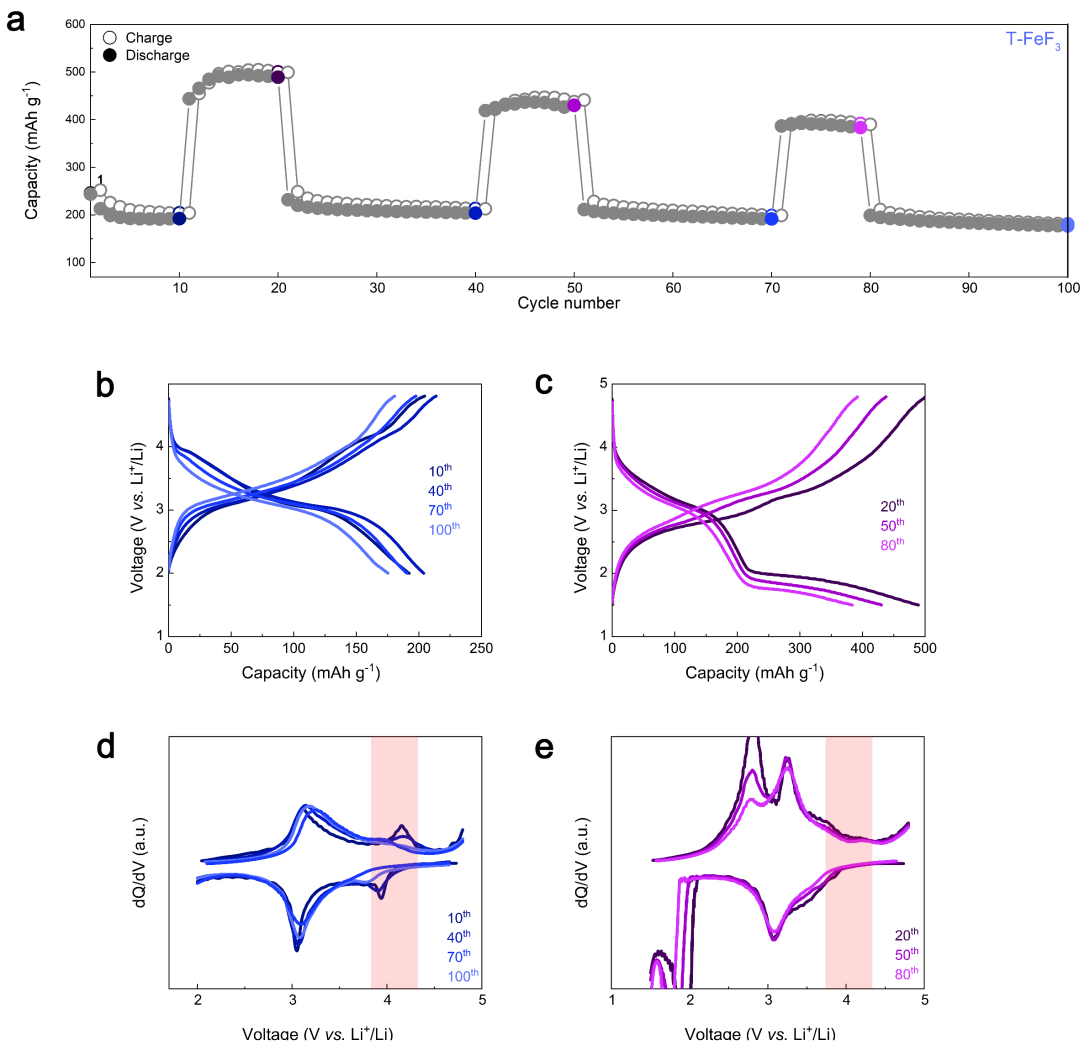

Supplementary Fig. S29. (a) Specific capacity of T-FeF_3 with repeated changed discharge cut-off voltage starting at 2 V discharge cut-off voltage. **(b)** Electrochemical profile and **(d)** differential analysis of voltage profile at 10^{th}, 40^{th}, 70^{th}, and 100^{th} cycle (voltage range: 4.8-2.0 V). **(c)** The charge/discharge profile and **(e)** differential analysis of voltage profile at 20^{th}, 50^{th}, and 80^{th} cycle (voltage range: 4.8-1.5 V).

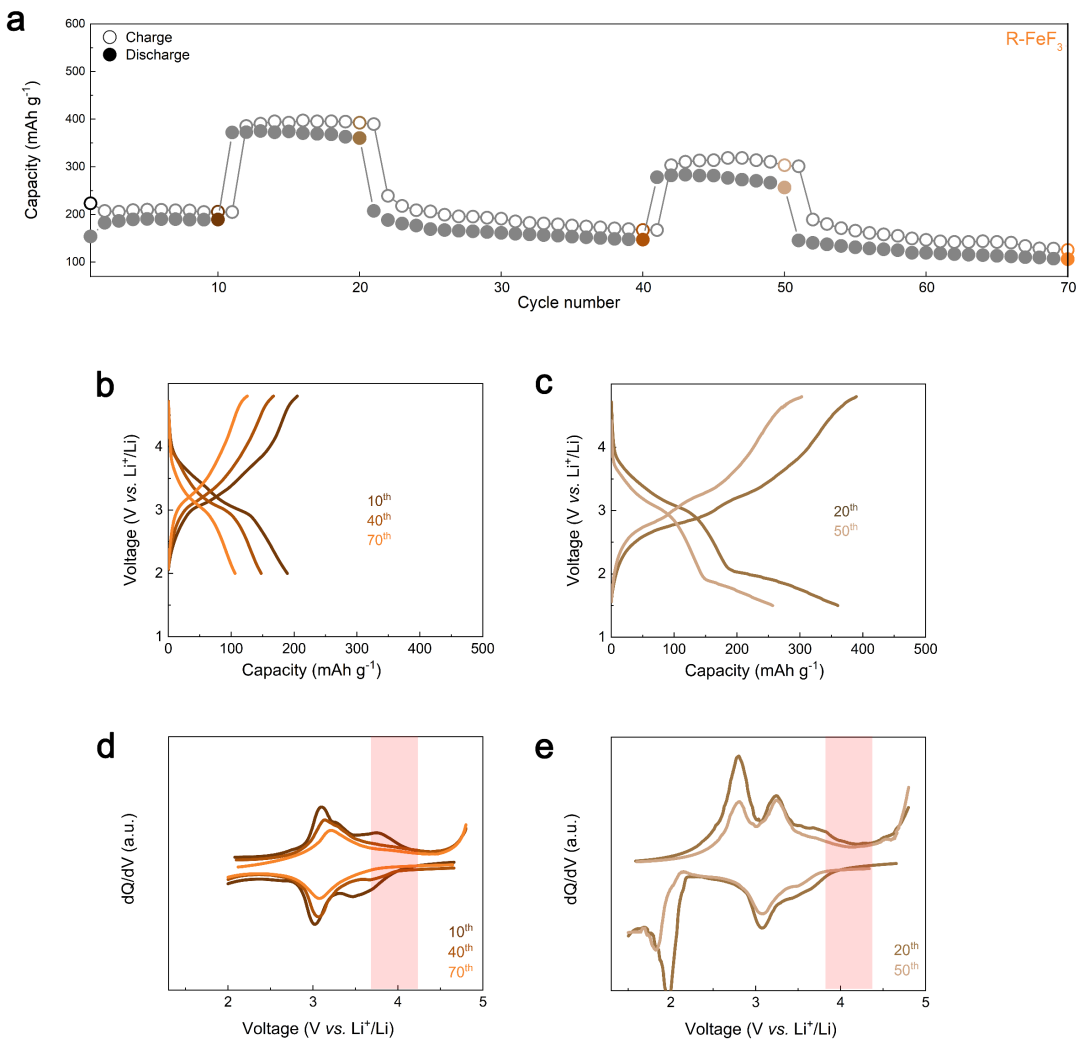

Supplementary Fig. S30. (a) Specific capacity of R-FeF_3 with repeated changed discharge cut-off voltage starting at 2 V discharge cut-off voltage. **(b)** Electrochemical profile and **(d)** differential analysis of voltage profile at 10^{th}, 40^{th}, and 70^{th} (voltage range: 4.8-2.0 V). **(c)** The charge/discharge profile and **(e)** differential analysis of voltage profile at 20^{th} and 50^{th} cycle (voltage range: 4.8-1.5 V).

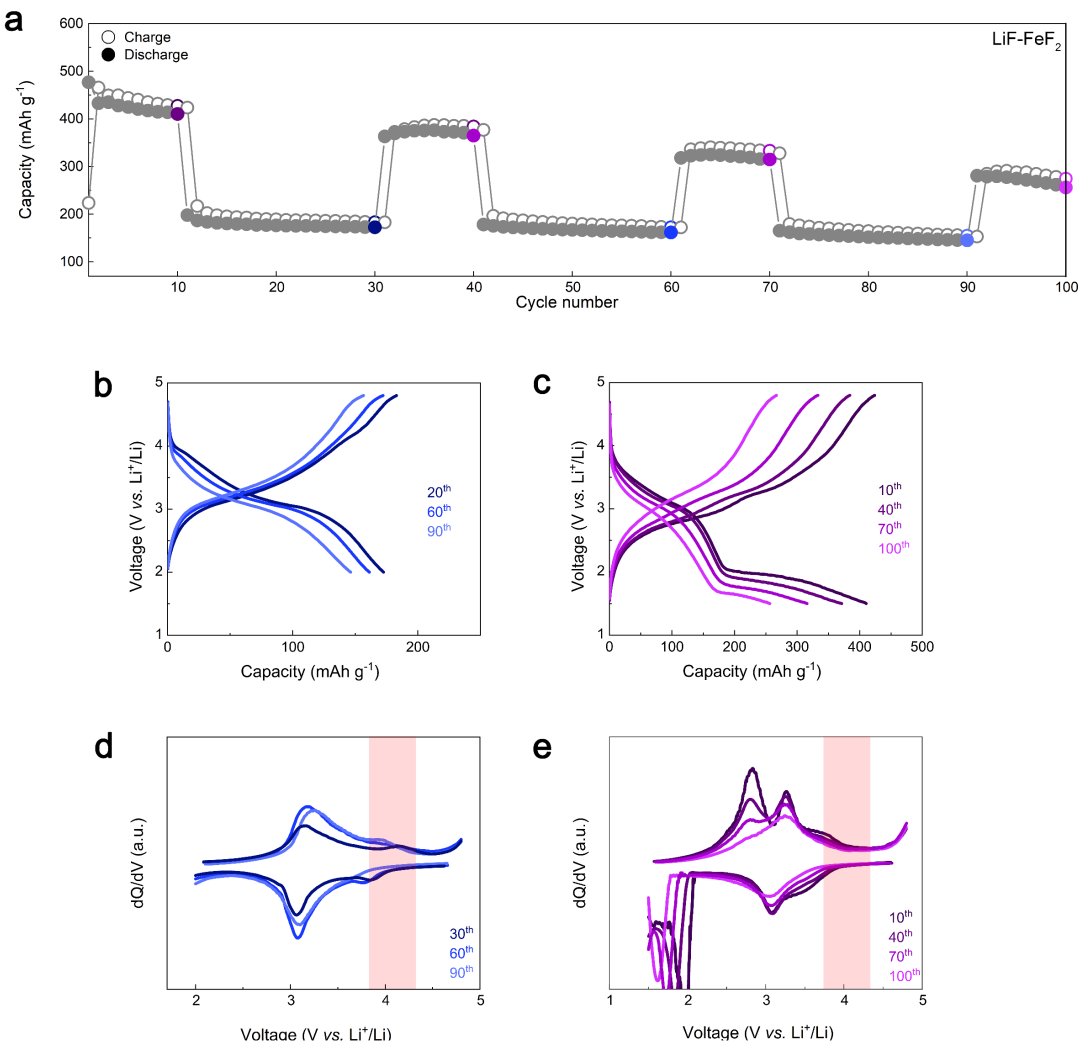

Supplementary Fig. S31. (a) Specific capacity of T-FeF_3 with repeated changed discharge cut-off voltage starting at 1.5 V discharge cut-off voltage. **(b)** Electrochemical profile and **(d)** differential analysis of voltage profile at 30^{th}, 60^{th}, and 90^{th} (voltage range: 4.8-2.0 V). **(c)** The charge/discharge profile and **(e)** differential analysis of voltage profile at 10^{th}, 40^{th}, 70^{th}, and 100^{th} cycle (voltage range: 4.8-1.5 V).

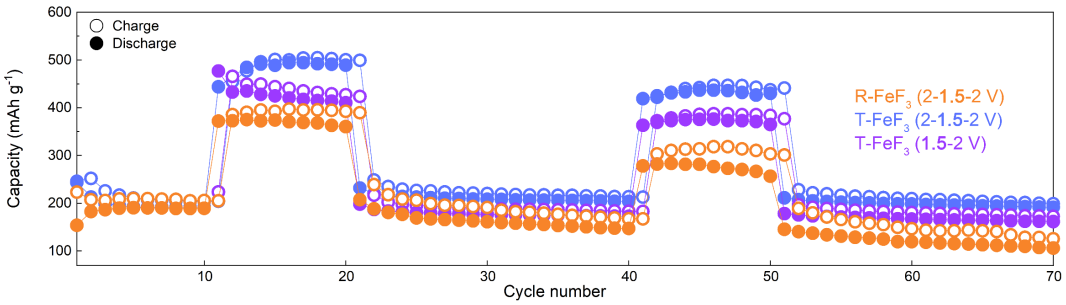

Supplementary Fig. S32. Comparison of specific capacities of T-FeF_3 and R-FeF_3 with repeated changes in depth of discharge.

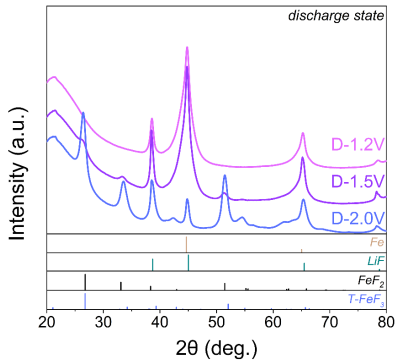

Supplementary Fig. S33. Comparison of XRD patterns of LiF-FeF_2 according to the depth of discharge. D and numbers represent discharge and discharge cut-off voltage, respectively. XRD measurement was performed after charging and discharging until the 10^{th} cycle where the electrochemical profile became uniform.

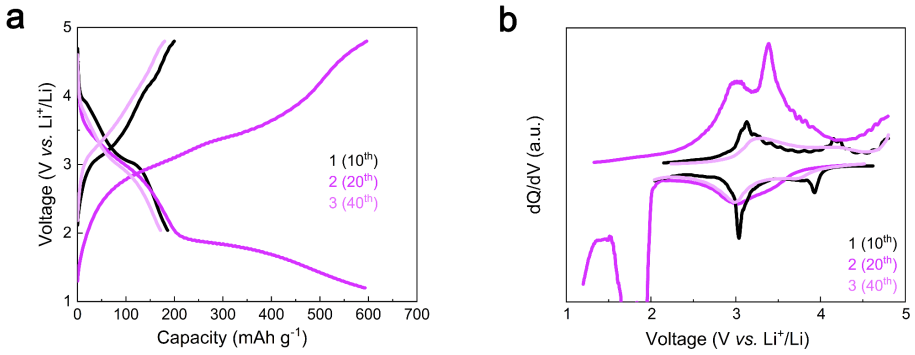

Supplementary Fig. S34. (a,b) Electrochemical profile and differential analysis of voltage profile for each point in Fig 5e.

Supplementary Table S1. Crystallographic parameters of LiF-FeF_2 nanocomposite obtained from Rietveld refinement**.**

Refinement result for LiF-FeF_2						
R-factor (%)						
Rp	R_{wp}	R_{exp}	$\chi 2$			
1.22	2.44	2.02	1.45			
Formula	space group		Fract. (%)			
FeF_2	*$P4_2/mnm$*		48.82			
Atom	site	x	y	z	occ.	
Fe	2a	0.0000	0.0000	0.0000	1.0000	
F	4f	0.1984	0.8016	0.5000	1.0000	
Lattice parameter (Å)						
a-axis	b-axis	c-axis	Volume ($Å^3$)	α	β	γ
4.7105	4.7105	3.2512	72.142	90	90	90
Formula	space group		Fract. (%)			
LiF	*Fm-3m*		51.18			
Atom	site	x	y	z	occ.	
Li	4a	0.0000	0.0000	0.0000	1.0000	
F	4b	0.0000	0.5000	0.0000	1.0000	
Lattice parameter (Å)						
a-axis	b-axis	c-axis	Volume ($Å^3$)	α	β	γ
4.0366	4.0366	4.0366	65.77	90	90	90

Supplementary Table S2. EXAFS structure parameters of the 10th charge state fitted to each structure.

structure	Path	N	ΔE (eV)	R (Å)	σ^2 (Å^2)	Reduced χ^2	R-factor
Ordered Tetragonal FeF_3	Fe-F_1	6	-2.85	1.921 ±0.003	0.0082 ±0.0006	161	0.025
	Fe-Fe_1	4	-2.85	3.690 ±0.022	0.0148 ±0.0032		
T-FeF_3	Fe-F_1	4	-2.79	1.926 ± 0.002	0.0032 ± 0.0003	12	0.003
	Fe-F_2	2	-2.79	2.141 ± 0.007	0.0082 ± 0.0014		
	Fe-Fe_1	2	-2.79	3.162 ± 0.004	0.0050 ± 0.0005		
	Fe-Fe_2	8	-2.79	3.688 ± 0.011	0.0253 ± 0.0018		
R-FeF_3	Fe-F_1	6	-2.39	1.925 ± 0.005	0.0106 ± 0.0008	224	0.037
	Fe-Fe_1	6	-2.39	3.754 ± 0.013	0.0107 ± 0.0012		

Supplementary Table S3. Crystallographic parameters of 10th charged state obtained from Rietveld refinement.

Refinement result for 10th charged state						
R-factor (%)						
Rp	R_{wp}	R_{exp}	$\chi 2$			
1.12	2.01	1.87	1.16			
Formula	space group		Fract. (%)			
$FeF_{2.96}$	*$P4_2/mnm$*		67.27			
Atom	site	x	y	z	occ.	
Fe	2a	0.0000	0.0000	0.0000	0.4240	
Fe	4e	0.0000	0.0000	0.3221	0.8030	
F	4f	0.3103	0.3103	0.0000	1.0000	
F	8j	0.3177	0.3177	0.3374	1.0000	
Lattice parameter (Å)						
a-axis	b-axis	c-axis	Volume ($Å^3$)	α	β	γ
4.6986	4.6986	9.4572	208.785	90	90	90
Formula	space group		Fract. (%)			
FeF_2	*$P4_2/mnm$*		7.61			
Atom	site	x	y	z	occ.	
Fe	2a	0.0000	0.0000	0.0000	1.0000	
F	4f	0.1984	0.8016	0.5000	1.0000	
Lattice parameter (Å)						
a-axis	b-axis	c-axis	Volume ($Å^3$)	α	β	γ
4.7132	4.7132	3.2487	72.167	90	90	90
Formula	space group		Fract. (%)			
LiF	*Fm-3m*		25.12			
Atom	site	x	y	z	occ.	
Li	4a	0.0000	0.0000	0.0000	1.0000	
F	4b	0.0000	0.5000	0.0000	1.0000	
Lattice parameter (Å)						
a-axis	b-axis	c-axis	Volume ($Å^3$)	α	β	γ
4.038	4.038	4.038	65.841	90	90	90

Supplementary Table S4. Crystallographic parameters of half-discharged state (point 2), 10th discharged state (point 3), and half-charged state (point 4) were obtained from Rietveld refinement. Each point is a point indicated in the voltage profile in Fig. 2b.

Refinement result for half-discharged state (point 2)						
R-factor (%)						
R_p	R_{wp}	R_{exp}	$\chi 2$			
1.12	1.93	1.85	1.09			
Formula	space group		Fract. (%)			
$Li_{0.31}FeF_{2.96}$	*P4₂/mnm*		67.45			
Atom	site	x	y	z	occ.	
Li	2a	0.0000	0.0000	0.0000	0.5600	
Li	4e	0.0000	0.0000	0.3305	0.0340	
Fe	2a	0.0000	0.0000	0.0000	0.3500	
Fe	4e	0.0000	0.0000	0.3305	0.8400	
F	4f	0.3481	0.3481	0.0000	1.0000	
F	8j	0.3171	0.3171	0.3501	1.0000	
Lattice parameter (Å)						
a-axis	b-axis	c-axis	Volume ($Å^3$)	α	β	γ
4.7012	4.7012	9.4884	209.7058	90	90	90
Formula	space group		Fract. (%)			
FeF_2	*P4₂/mnm*		7.44			
Atom	site	x	y	z	occ.	
Fe	2a	0.0000	0.0000	0.0000	1.0000	
F	4f	0.1984	0.8016	0.5000	1.0000	
Lattice parameter (Å)						
a-axis	b-axis	c-axis	Volume ($Å^3$)	α	β	γ
4.7107	4.7107	3.2513	72.147	90	90	90
Formula	space group		Fract. (%)			
LiF	*Fm-3m*		25.11			
Atom	site	x	y	z	occ.	
Li	4a	0.0000	0.0000	0.0000	1.0000	
F	4b	0.0000	0.5000	0.0000	1.0000	
Lattice parameter (Å)						
a-axis	b-axis	c-axis	Volume ($Å^3$)	α	β	γ
4.0377	4.0377	4.0377	65.826	90	90	90

Refinement result for 10th discharged state (point 3)			
R-factor (%)			
R_p	R_{wp}	R_{exp}	$\chi 2$
1.06	2.03	1.75	1.34

Formula	space group		Fract. (%)			
Li0.30FeF2.59	*P4₂/mnm*		13.86			
Atom	site	x	y	z	occ.	
Li	2a	0.3284	0.3284	0.0000	1.0000	
Li	4e	0.3122	0.3122	0.3366	1.0000	
Fe	2a	0.0000	0.0000	0.0000	0.3930	
Fe	4e	0.0000	0.0000	0.3134	0.9600	
F	4f	0.0000	0.0000	0.0000	0.6020	
F	8j	0.0000	0.0000	0.3134	0.0400	
Lattice parameter (Å)						
a-axis	b-axis	c-axis	Volume (Å^3)	α	β	γ
4.7394	4.7394	9.6472	216.695	90	90	90
Formula	space group		Fract. (%)			
FeF_2	*P4₂/mnm*		34.59			
Atom	site	x	y	z	occ.	
Fe	2a	0.0000	0.0000	0.0000	1.0000	
F	4f	0.1984	0.8016	0.5000	1.0000	
Lattice parameter (Å)						
a-axis	b-axis	c-axis	Volume (Å^3)	α	β	γ
4.7120	4.7120	3.2514	72.192	90	90	90
Formula	space group		Fract. (%)			
LiF	*Fm-3m*		51.55			
Atom	site	x	y	z	occ.	
Li	4a	0.0000	0.0000	0.0000	1.0000	
F	4b	0.0000	0.5000	0.0000	1.0000	
Lattice parameter (Å)						
a-axis	b-axis	c-axis	Volume (Å^3)	α	β	γ
4.0361	4.0361	4.0361	65.749	90	90	90

Refinement result for half-charge state (point 4)						
R-factor (%)						
R_p	R_{wp}	R_{exp}	$\chi 2$			
1.2	2.02	1.84	1.20			
Formula	space group		Fract. (%)			
Li0.05FeF2.83	*P4₂/mnm*		32.88			
Atom	site	x	y	z	occ.	
Li	2a	0.0000	0.0000	0.0000	0.0870	
Li	4e	0.0000	0.0000	0.3355	0.0120	
Fe	2a	0.0000	0.0000	0.0000	0.3630	
Fe	4e	0.0000	0.0000	0.3355	0.8780	
F	4f	0.3295	0.3295	0.0000	1.0000	

F	8j	0.3250	0.3250	0.3480	1.0000	
Lattice parameter (Å)						
a-axis	b-axis	c-axis	Volume ($Å^3$)	α	β	γ
4.7328	4.7328	9.6119	215.301	90	90	90
Formula	space group		Fract. (%)			
FeF_2	*$P4_2/mnm$*		25.04			
Atom	site	x	y	z	occ.	
Fe	2a	0.0000	0.0000	0.0000	1.0000	
F	4f	0.1984	0.8016	0.5000	1.0000	
Lattice parameter (Å)						
a-axis	b-axis	c-axis	Volume ($Å^3$)	α	β	γ
4.7132	4.7132	3.2569	72.349	90	90	90
Formula	space group		Fract. (%)			
LiF	*Fm-3m*		42.08			
Atom	site	x	y	z	occ.	
Li	4a	0.0000	0.0000	0.0000	1.0000	
F	4b	0.0000	0.5000	0.0000	1.0000	
Lattice parameter (Å)						
a-axis	b-axis	c-axis	Volume ($Å^3$)	α	β	γ
4.0387	4.0387	4.0387	65.873	90	90	90

Supplementary Table S5. Comparison of previously reported iron fluoride materials composited with carbon.

No.	ref.	sample	Theoretical	Initial discharge	Cycling nunber	Current ($mA\ g^{-1}$)	Post-cycle discharge	capacity retention	Voltage range
			Capacity ($mAh\ g^{-1}$)	Capacity ($mAh\ g^{-1}$)			capacity ($mAh\ g^{-1}$)		
1	*ACS Appl. Mater. Interfaces,* **2019**, 11, 30959-30967.	FeF_3/C (70:25)	712 (3Li)	650	30	71.2	360	55.40%	1.0-4.5V
				620			200	32.30%	
				650			200	30.80%	
				645			360	55.80%	
2	*J. Mater. Eng. Perform.*, **2018**, 27, 624-629.	FeF_3	712 (3Li)	210.51	40	50	54.42	25.90%	1.0-4.0V
		FeF_3/AB(85:15)		346.25			161.58	46.70%	
3	*Chem. Commun*., **2012**, 48, 9909-9911	FeF_3–H-rGO	712 (3Li)	690	110	100	200	29.00%	1.0-4.5V
		FeF_3		520			90	17.30%	
4	*J. Fluorine Chem*., **2016**, 184, 75-81	FeF_3/AB (70:25)	712 (3Li)	510	15	71.2	180	35.30%	1.0-4.5V
5	*FlateChem*, **2022**, 33, 100360.	FeF_3/C-SWNT	712 (3Li)	300	100	300	190	63.33%	1.0-4.5V
		FeF_3		200			60	30.00%	1.0-4.0V
6	Ionics, **2018**, 24, 1561–1569	FeF_3/C	475 (2Li)	170	53	20	89	52.40%	1.5-4.5V
7	*ACS Appl. Mater. Interfaces.,* **2017**, 9, 17992-18000.	bare FeF_3	475 (2Li)	598	170	100	80	13.40%	1.5-4.5V
8	*J. Alloy. Compd*., **2015**, 647, 750-755.	FeF_3/r-GO1.7	237 (1Li)	195	50	23.7	170	87.18%	2.0–4.5 V
			475 (2Li)	414		71.2	274	66.18%	1.5–4.5 V
		FeF_3	237 (1Li)	114		23.7	50	43.86%	2.0–4.5 V
			475 (2Li)	314		71.2	35	11.15%	1.5–4.5 V
9	*RSC Adv*., **2014**, 4, 6730-6737.	FeF_3	712 (3Li)	710	12	14.3	140	19.72%	1.5–4.5 V
10	*J. Mater. Chem*., **2012**, 22, 17539-17550.	FeF_3/AB (85:15)	237 (1Li)	129.3	100	237	101.9	78.80%	2.0V-4.5V
				119		474	83.6	70.30%	
				105.1		1185	71.2	67.70%	
11	*J. Mater. Chem*., **2011**, 21, 10035-10041.	FeF_3/AB (70:25)	237 (1Li)	210	25	10	100	47.60%	2.0V-4.5V
		FeF_3/AB-HT		200	50	10	168	84.00%	
12	Chem. Commun., **2016**, 52, 9414-9417	FeF_3/C composite	237 (1Li)	170	100	250	127	74.71%	2.0-4.5V
13	*ChemElectroChem*, **2019**, 6, 5203- 5210.	FeF_3	237 (1Li)	40	200	474	30	75.00%	2.0-4.5V
		FCO (FeF_3@carbon nanocomposite)		120			45	37.50%	
		FCN (FeF_3@N-doped carbon nanocomposite)		140			100	71.43%	

REFERENCES

1. Vinogradov, A. S. *et al.* Low-lying unoccupied electronic states in 3d transition-metal fluorides probed by NEXAFS at the F 1s threshold. *Phys. Rev. B - Condens. Matter Mater. Phys.* **71**, 1–11 (2005).
2. Sina, M. *et al.* Structural phase transformation and Fe valence evolution in FeO xF2-x/C nanocomposite electrodes during lithiation and de-lithiation processes. *J. Mater. Chem. A* **1**, 11629–11640 (2013).
3. Vinogradov, A. S. *et al.* Low-lying unoccupied electronic states in 3d transition-metal fluorides probed by NEXAFS at the F 1s threshold. *Phys. Rev. B - Condens. Matter Mater. Phys.* **71**, (2005).
4. Cosandey, F., Su, D., Sina, M., Pereira, N. & Amatucci, G. G. Fe valence determination and Li elemental distribution in lithiated FeO 0.7F 1.3/C nanocomposite battery materials by electron energy loss spectroscopy (EELS). *Micron* **43**, 22–29 (2012).
5. GOOD, G. Core-exciton absorption in the F K absorption spectra of 3d transition-metal fluorides. Phys. *Phys. Rev. B - Condens. Matter Mater. Phys.* **37**, 10895−10897 (1988).
6. Zheng, Y. *et al.* Phase Evolution of Trirutile Li0.5FeF3 for Lithium-Ion Batteries. *Chem. Mater.* **33**, 868–880 (2021).
7. Kityakarn, S., Worayingyong, A., Suramitr, A. & Smith, M. F. Ce-doped nanoparticles of TiO2: Rutile-to-brookite phase transition and evolution of Ce local-structure studied with XRD and XANES. *Mater. Chem. Phys.* **139**, 543–549 (2013).
8. Jung, S. K. *et al.* Lithium-free transition metal monoxides for positive electrodes in lithium-ion batteries. *Nat. Energy* **2**, (2017).
9. Wei, K. *et al.* Low-Overpotential LiF Splitting in Lithiated Fluoride Conversion Cathode Catalyzed by Spinel Oxide. *Adv. Funct. Mater.* **31**, 2009133 (2021).
10. Tomita, Y. *et al.* Synthesis and charge-discharge properties of LiF-NiO composite as a cathode material for Li-ion batteries. *J. Power Sources* **329**, 406–411 (2016).
11. Tomita, Y. *et al.* Synthesis and electrochemical properties of 4LiF-NiMn2O4 composite as a cathode material for Li-ion batteries. *J. Power Sources* **354**, 34–40 (2017).
12. Dimov, N., Kitajou, A., Hori, H., Kobayashi, E. & Okada, S. Electrochemical Splitting of Lif: A New Approach to Lithium-Ion Battery Materials. *ECS Meet. Abstr.* **58**, 87–99 (2014).
13. Hua, X. *et al.* Revisiting metal fluorides as lithium-ion battery cathodes. *Nat. Mater.* **20**, 841–850 (2021).
14. Jain, A. *et al.* Commentary: The materials project: A materials genome approach to accelerating materials innovation. *APL Mater.* **1**, 011002 (2013).
15. Li, L. *et al.* Origins of Large Voltage Hysteresis in High-Energy-Density Metal Fluoride Lithium-Ion Battery Conversion Electrodes. *J. Am. Chem. Soc.* **138**, 2838–

2848 (2016).

16. Li, L. *et al.* Visualization of electrochemically driven solid-state phase transformations using operando hard X-ray spectro-imaging. *Nat. Commun.* **6**, 6883 (2015).

17. Li, L., Meng, F. & Jin, S. High-capacity lithium-ion battery conversion cathodes based on iron fluoride nanowires and insights into the conversion mechanism. *Nano Lett.* **12**, 6030–6037 (2012).

18. Wang, F. *et al.* Ternary metal fluorides as high-energy cathodes with low cycling hysteresis. *Nat. Commun.* **6**, 6668 (2015).

19. Wang, F. *et al.* Conversion reaction mechanisms in lithium ion batteries: Study of the binary metal fluoride electrodes. *J. Am. Chem. Soc.* **133**, 18828–18836 (2011).